

XDen-1K: A Density Field Dataset of Real-World Objects

Jingxuan Zhang* Tianqi Yu* Yatu Zhang* Jinze Wu Kaixin Yao Jingyang Liu
Yuyao Zhang[†] Jiayuan Gu[†] Jingyi Yu[†]
ShanghaiTech University

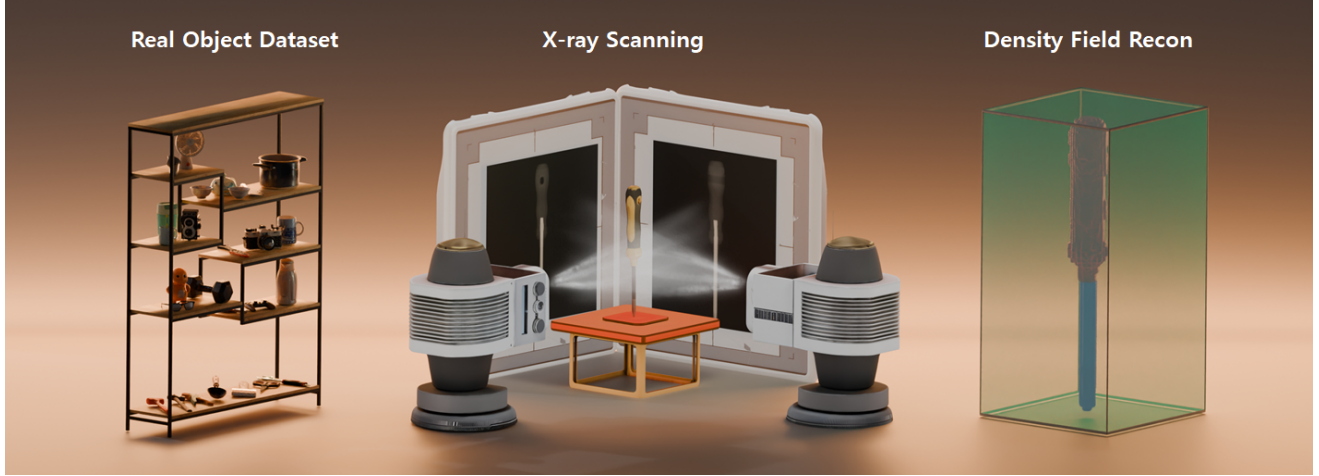


Figure 1. We present XDen-1K, a multi-modal dataset of real-world objects, featuring paired biplanar X-ray scans and reconstructed density fields.

Abstract

A deep understanding of the physical world is a central goal for embodied AI and realistic simulation. While current models excel at capturing an object’s surface geometry and appearance, they largely neglect its internal physical properties. This omission is critical, as properties like volumetric density are fundamental for predicting an object’s center of mass, stability, and interaction dynamics in applications ranging from robotic manipulation to physical simulation. The primary bottleneck has been the absence of large-scale, real-world data. To bridge this gap, we introduce XDen-1K, the first large-scale, multi-modal dataset designed for real-world physical property estimation, with a particular focus on volumetric density. The core of this dataset consists of 1,000 real-world objects across 148 categories, for which we provide comprehensive multi-modal data, including a high-resolution 3D geometric model with part-level annotations and a corresponding set of real-world biplanar X-ray scans. Building upon this data, we

introduce a novel optimization framework that recovers a high-fidelity volumetric density field of each object from its sparse X-ray views. To further enhance the dataset’s versatility, we have additionally annotated approximately 7.6k synthetic objects and collected 20 CT scans, successfully integrating the real-world X-ray scans, high-precision CT validation, and large-scale synthetic data. To demonstrate its practical value, we add X-ray images as a conditioning signal to an existing segmentation network and perform volumetric segmentation. Furthermore, we conduct experiments on downstream robotics tasks. The results show that leveraging the dataset can effectively improve the accuracy of center-of-mass estimation and the success rate of robotic manipulation. We believe XDen-1K will serve as a foundational resource and a challenging new benchmark, catalyzing future research in physically grounded visual inference and embodied AI. Our webpage is available at <https://xden-1k.github.io/>

1. Introduction

Objects are more than their appearance: beyond color and texture, they possess internal composition — materials, thickness, voids, reinforcements, and mass distribution — that determine how they function, fail, and can

* Authors contributed equally to this work. [†] The corresponding authors are Yuyao Zhang (zhangyy8@shanghaitech.edu.cn), Jiayuan Gu (gujy1@shanghaitech.edu.cn), Jingyi Yu (yujingyi@shanghaitech.edu.cn).

be used. Modeling these physical attributes, coupled with visual inferences of shape and texture, enables more reliable physical reasoning [3, 28, 49], physically-based simulations [9, 25], and, most recently, object and scene reconstructions [44, 48]. For robots, these “hidden” properties are particularly useful for inferring where mass is concentrated [2, 37] (center of mass, moments of inertia), how stiff or compliant parts are, what forces and grasps are safe and effective, how objects will deform or fracture, which tools to use, etc.

Humans infer physical properties by combining visual cues (multi-view geometry, symmetry, material priors) and interactions (e.g. sound, deformation, context) [19, 24, 40, 41, 47, 52]. At the surface level, recent success in material-property estimation [13, 22, 32] (e.g. SVBRDF/BSDF, albedo/roughness, microgeometry) is largely attributed to the availability of controlled, large-scale visual datasets. Density, in contrast, is inherently volumetric and, thereby, “invisible” to regular RGB cameras. The latest efforts [1, 7, 46] have focused on labeling parts by associating their appearance with material types. The resulting datasets are therefore synthetic and lack real-world validation. A real-world density dataset will facilitate learning in physically meaningful units, expose models to realistic multi-material mixtures and manufacturing artifacts. It also provides the urgently needed common benchmarks for current and future visual inference tasks.

In this paper, we present **XDden-1K**: an X-ray imaging based **density field dataset** of **1,000** real-world objects. XDden-1K is the first of its type, with objects covering sizes from small hardware (e.g. screw, flashlight, key) to medium household goods (e.g. kettle, bicycle helmet, power tool at $\sim 20\text{--}30$ cm), and to larger items (e.g. cookware, sports equipment, furniture). The most direct brute-force approach to acquiring a ground-truth density field is computed tomography (CT), which was initially developed for medical and industrial inspection. However, high-resolution CT is time-consuming and costly—typical scans take 15–60 minutes and can cost \$100–\$500 per object, so 1,000 objects imply hundreds to thousands of scanner-hours and a six-figure budget. Even with CT, the so-called beam hardening effect will make recovering internal information more difficult.

We begin by reconstructing the density field from biplanar X-rays. To constrain the highly underdetermined reconstruction problem, we incorporate manually annotated object parts that provide prior knowledge of each part’s size, shape, and boundaries. Each part is assumed to consist of a homogeneous material, thereby greatly reducing the dimensionality of the solution space compared with pixel-wise optimization methods. Under specified X-ray energy conditions, the material density was approximated by its corresponding linear attenuation coefficient (LAC). Using

this algorithm, we recovered approximate density fields for 1,000 real biplanar X-ray samples and constructed a new dataset, XDden-1K. To test the result of our reconstruction, we collect a small-scale CT dataset and evaluate the density of each part.

Based on XDden-1K, our paired X-ray and density field dataset, we introduce two subtasks: X-ray conditioned volumetric segmentation and CoM-aware robot manipulation. These two tasks take great advantage of our data, where X-ray provides great structural and material prior and density field provides physical information on both static (mass, center of mass) and dynamic (moment of inertia) properties of an object.

Our contributions:

1. We propose the **XDden-1K** dataset, the first large-scale real-world object dataset, coupled with both **biplanar X-ray images** and **density fields**.
2. We develop an X-ray optimization algorithm to analyze the material type of each segmented part in a physically plausible way and validate it with a small CT subset.
3. We further demonstrate the value of X-ray as an additional modality. By conditioning an existing volumetric segmentation model on X-ray images, we obtain improved volumetric segmentation performance on both real and simulated data.
4. We additionally prove that a good estimation of density and mass can lead to higher accuracy in embodied AI tasks. Our provided density field data serves as a benchmark for future embodied grasping tasks.

2. Related Work

Density Inference and Physics-Aware Modeling. A broad line of work seeks to endow 3D vision with physical awareness by predicting material or density-related properties directly from visual input [8, 21, 27, 29, 45, 46, 51]. Optimization-based approaches combine differentiable physics with neural scene representations to fit elastic or material parameters from observed motion, but they are typically evaluated on synthetic or tightly controlled setups, making it unclear how well they transfer to real objects. More recent feed-forward methods instead regress spatially varying material fields from learned 3D features. PIXIE [27], for example, learns a supervised mapping from distilled feature volumes to per-voxel material parameters, while GaussianProperty [46] assigns physical attributes to 3D Gaussians using segmentation and vision-language priors. Collectively, these methods demonstrate that appearance encodes rich physical cues, but in the absence of real volumetric ground truth, their predictions remain difficult to rigorously validate. Works like PhysX-3D [7] and PhysX-Anything [8] aim to build physics-ready assets for simulation and also augment large 3D model collections with

absolute scale, material categories, affordances, and kinematic attributes. Datasets like 3DCoMPaT200 [1] contain large amounts of 3D assets and their material composition.

These resources mark an important step toward learning physically grounded representations; yet, they are constructed from synthetic or curated 3D assets and rely on assumed or inferred physical properties rather than measurements. None provide large-scale, real-world volumetric density fields against which both prediction methods and physics-aware generative models can be quantitatively evaluated. In contrast, our XDden-1K dataset is built from calibrated biplanar X-ray measurements, offering empirically grounded density fields for 1,000 real objects and furnishing the missing real-world benchmark for volumetric density estimation.

X-ray and CT imaging. X-rays are high-energy electromagnetic waves characterized by high photon energy and a low probability of interaction with matter. Unlike infrared or visible light, which are easily absorbed or reflected at the surface, X-rays can penetrate most materials and reveal internal structures without causing damage [17]. This strong penetration capability enables the observation and reconstruction of 3D material distributions from 2D projections. Computed Tomography (CT), as one of the most accurate 3D reconstruction techniques, acquires dense angular projections—collectively referred to as a sinogram—by scanning an object from multiple viewpoints. Classical reconstruction algorithms [15, 30, 35, 36] can effectively recover volumetric information from these dense sinograms. Consequently, CT reconstruction plays a crucial role in medical diagnosis, industrial defect detection, and scientific imaging [16, 38].

However, a CT scan often incurs high acquisition cost and long scanning time, while traditional algorithms suffer from severe streak and beam-hardening artifacts in the presence of high-density materials. Considerable research has therefore focused on reducing CT scan time via sparse-view CT reconstruction, which lowers the number of projection angles required for reconstruction. For example, SAX-NeRF [6] and SCOPE [43] use continuum modeling based on Neural Radiance Fields (NeRF) [34], where sparse angular projections are constrained and fused with viewpoints in an implicit space, thereby filling in missing viewpoint information in the learned dense volume representation. Nevertheless, at least dozens of projections are typically required to achieve acceptable quality; otherwise, strong sparse artifacts remain inevitable.

To further reduce acquisition time and radiation dose, biplanar X-ray imaging has emerged as a promising alternative [33]. By simultaneously projecting from two orthogonal viewpoints, this technique partially compensates for the loss of depth information inherent in single-view X-rays.

Number of categories	148
Average number of parts per obj.	4.94
Average scanning time	2 s
Total amount of real data	1,000
Size limit	$\leq 70 \text{ cm} \times 35 \text{ cm} \times 35 \text{ cm}$

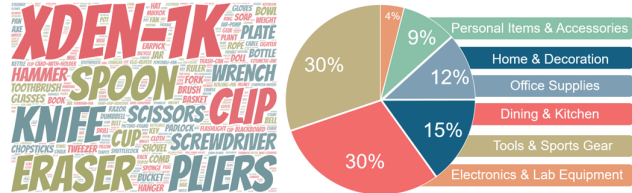


Figure 2. **Statistics of XDden-1K.** It contains 1,000 everyday objects, covering 148 categories.

Recent advances have demonstrated its potential in clinical diagnosis [4, 10], providing richer structural cues and improved diagnostic accuracy compared to single-view X-ray imaging. Several studies have explored reconstructing 3D CT-like volumes from biplanar X-rays using either generative models [23, 50] or regression-based mapping networks [20, 26]. These approaches highlight the feasibility of biplanar imaging as a low-cost, low-time, and low-dose substitute for traditional CT. However, they typically rely on large paired datasets of high-quality CT and corresponding X-rays for supervision. For non-medical objects where such paired data are unavailable, how to effectively incorporate prior knowledge and achieve faithful 3D reconstruction remains a challenging open problem.

Part-Level Understanding. Parts, viewed as the compositional units of an object, carry rich structural and semantic relationships. Existing 3D part-understanding methods predominantly operate on surface representations: some take point clouds as input for semantic or instance-level part segmentation, while others process meshes for surface segmentation or part-based generation [31, 39, 53, 54]. Building on these advances, we can obtain accurate mesh-level segmentation. Most existing methods focus on occupancy or semantic voxel labeling rather than physically grounded part decomposition [11, 12, 14, 18]. We introduce X-ray images as an additional conditioning signal: thanks to its strong priors on internal structure, thickness, and density, we have the ability to produce more reasonable, physically consistent voxel-level segmentation.

3. XDden-1K Dataset

3.1. Overview

XDden-1K is a large-scale dataset of 1,000 real-world objects constructed to advance the study of volumetric density

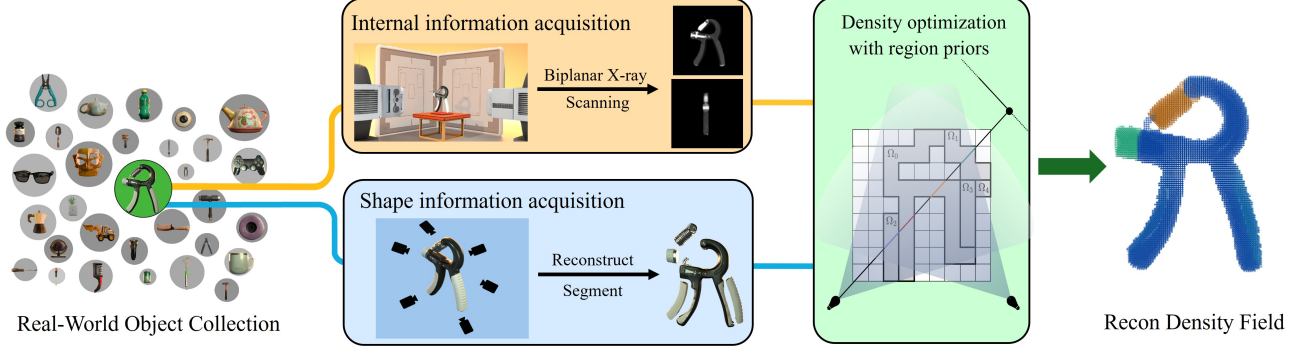


Figure 3. **Overview of XDen-1K generation pipeline.** Multi-view RGB images are used to reconstruct a surface mesh, and manually labeled segments provide accurate part-level shape information. Orthogonal biplanar X-rays capture internal attenuation signals. The recovered shape priors are then incorporated into an X-ray optimization process to estimate the volumetric density field.

estimation and part-level physical understanding. The collection spans 148 categories, covering a broad spectrum of everyday items such as tools, kitchenware, and consumer electronics, providing rich variation in geometry, size, materials, and internal structure. Objects are deliberately chosen to be both common in real-world manipulation and diverse in internal composition, including solid, hollow, layered, and composite structures. Each object in the dataset is captured and annotated through a standardized pipeline. We first preprocess the object to obtain its real-world scale, reconstruct the mesh and perform a human-in-the-loop segmentation (Sec. 3.2) that serves as a reliable structural prior for subsequent X-ray-based volumetric density reconstruction. We then collect paired biplanar X-ray scans (Sec. 3.3) and reconstruct a volumetric density field (Sec. 3.4) that is physically consistent with both the mesh and the measured attenuation. To validate the fidelity of our reconstruction process, a subset of complex objects was also scanned using high-resolution CT.

For each object, we provide a part-segmented 3D mesh, biplanar X-ray scans, and a reconstructed volumetric density field. A subset of objects also includes high-resolution CT scans for validation. This multi-modal collection establishes a physically-grounded benchmark for training and evaluating models that jointly reason about geometry, part composition, and volumetric density. Comprehensive statistics are summarized in Figure 2.

3.2. Preprocessing

To preprocess each object into a physically grounded geometric representation, we first capture calibrated multi-view RGB images and reconstruct a watertight mesh in an arbitrary canonical scale. We then measure the physical dimensions of the object and apply a global scaling to align the mesh with real-world metric units. Finally, we annotate part-level segmentations on the mesh to decompose objects into semantically and functionally meaningful com-

ponents. All the preprocessing yields a metrically accurate, part-aware geometric representation of the object that serves as the structural prior and reference frame for subsequent biplanar X-ray acquisition and volumetric density reconstruction.

3.3. Preliminary: X-ray Imaging

X-rays possess the ability to penetrate matter. When an X-ray beam passes through an object, its intensity attenuates exponentially according to the Beer-Lambert law. For a ray \mathbf{r} traversing a volumetric object, the detected intensity I is related to the incident intensity I_0 as

$$I = I_0 e^{-\int_L \mu(x) dx}, \quad (1)$$

where $\mu(x)$ denotes the linear attenuation coefficient (LAC) at spatial location x , which characterizes the probability per unit length that an X-ray photon is absorbed or scattered by the material. Taking the logarithm of both sides yields the projection measurement p :

$$p = -\ln \left(\frac{I}{I_0} \right) = \int_L \mu(x) dx, \quad (2)$$

which corresponds to the line integral of the LAC along the ray trajectory. In practice, the detector measures the transmitted intensity I , and the reference air-scan intensity I_0 is pre-calibrated. The logarithmic transformation converts the exponential attenuation into a linear integral form, establishing the foundation of tomographic reconstruction. During reconstruction, the objective is to invert Eq. (2) over all rays to recover the 3D spatial distribution of $\mu(x)$, the LAC field. Classical algorithms such as Filtered Backprojection (FBP) in CT reconstruction are effective when projections are densely sampled over viewing angles. Once $\mu(x)$ is reconstructed, it serves as a quantitative descriptor of material composition and density. Physically, the LAC depends on both the density, ρ , and the mass attenuation coefficient

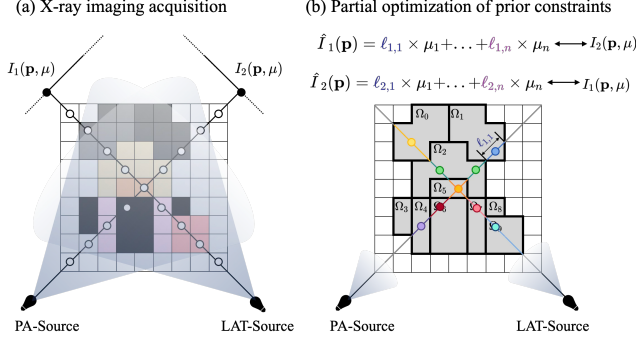


Figure 4. Differentiable rendering optimization

(MAC), $\frac{\mu}{\rho}(E)$, which is a material-dependent quantity determined by atomic composition and photon energy E :

$$\mu(E) = \rho \cdot \frac{\mu}{\rho}(E). \quad (3)$$

According to reference database XCOM [5] from the National Institute of Standards and Technology (NIST), the MACs of most common materials (e.g., water, polymers, biological tissues) converge to approximately $0.17 \text{ cm}^2/\text{g}$ at a certain energy level (e.g., 100 keV), as detailed in Table 1. Consequently, for such materials, μ exhibits an approximately linear relationship with density, enabling direct density estimation from reconstructed LAC values:

$$\rho = \frac{\mu}{(\mu/\rho)} = \frac{\mu}{0.17}. \quad (4)$$

This principle underpins quantitative X-ray imaging, allowing reconstructed attenuation maps to be interpreted as physically meaningful density fields.

In actual biplanar X-ray acquisition, we used the Eagle Eye biplanar X-ray imaging system developed by TaoImage. We used a 100 kV tube voltage, a 450 mA tube current, an exposure time of 280 ms per exposure, and a total exposure of 126 mAs.

Table 1. Mass attenuation coefficient (MAC), density, and linear absorption coefficient (LAC) of representative materials at 100 keV ray energy.

Material	Chemical Formula	MAC (cm ² /g)	Density (g/cm ³)	LAC (cm ⁻¹)
Water	H ₂ O	0.17	1.00	0.17
Air	N ₂ , O ₂	0.15	0.0012	1.8×10^{-4}
Glass	SiO ₂	0.18	2.40	0.432
Plastic (PP)	(C ₃ H ₆) _n	0.18	0.90	0.16
Plastic (PVC)	(C ₂ H ₃ Cl) _n	0.18	1.40	0.25
Rubber	(C ₅ H ₈) _n	0.19	1.20	0.22
Wood	C ₆ H ₁₀ O ₅	0.16	0.80	0.12
Aluminum	Al	0.19	2.70	0.51

3.4. Reconstruction Algorithms

While computed tomography (CT) provides accurate 3D reconstructions, its high cost and long acquisition times make it prohibitive for large-scale datasets. In contrast, single-plane X-ray imaging is faster and more economical, yet it completely loses depth information by integrating attenuation coefficients along the projection direction. Consequently, recovering a 3D density field from a single X-ray projection is a severely ill-posed inverse problem. We therefore adopt a pragmatic approach that utilizes two orthogonal, biplanar X-ray projections, regularized by a strong geometric prior. This strategy leverages the complementary depth cues from the two projections and constrains the solution space through known geometry, thereby making the reconstruction problem tractable.

We assume a given segmentation, represented by a set of K disjoint regions $\{\Omega_k\}_{k=1}^K$, each corresponding to a homogeneous material with a constant linear attenuation coefficient (LAC) μ_k . The volumetric attenuation field $\mu(\mathbf{x})$ is thus modeled as a piecewise-constant function:

$$\mu(\mathbf{x}) = \sum_{k=1}^K \mu_k \mathbf{1}_{\Omega_k}(\mathbf{x}), \quad (5)$$

where $\mathbf{1}_{\Omega_k}(\mathbf{x})$ is the indicator function:

$$\mathbf{1}_{\Omega_k}(\mathbf{x}) = \begin{cases} 1, & \text{if } \mathbf{x} \in \Omega_k, \\ 0, & \text{otherwise.} \end{cases}$$

Let $\mathcal{L}_i(\mathbf{p})$ denote the ray of biplanar X-ray acquisition geometry corresponding to pixel \mathbf{p} on detector plane $i \in \{1, 2\}$. The measured intensity $I_i(\mathbf{p})$ at pixel \mathbf{p} follows Eq. 2.

Substituting Eq. (5) into Eq. (2), the integral can be decomposed into region-wise path lengths:

$$\hat{I}_i(\mathbf{p}) = I_0 \exp\left(-\sum_{k=1}^K \mu_k \ell_{i,k}(\mathbf{p})\right), \quad (6)$$

where $\ell_{i,k}(\mathbf{p}) = \int_{\mathcal{L}_i(\mathbf{p}) \cap \Omega_k} dx$ denotes the path length of ray $\mathcal{L}_i(\mathbf{p})$ through region Ω_k . This quantity can be precomputed geometrically from the known part segmentation and projection geometry.

The reconstruction task then reduces to estimating the material-wise attenuation vector $\boldsymbol{\mu} = [\mu_1, \mu_2, \dots, \mu_K]^\top$. We jointly minimize the discrepancy between the simulated and measured projections from both biplanar views:

$$\hat{\boldsymbol{\mu}} = \arg \min_{\boldsymbol{\mu}} \sum_{i=1}^2 \sum_{\mathbf{p}} \left| I_i(\mathbf{p}; \boldsymbol{\mu}) - \tilde{I}_i(\mathbf{p}) \right|_2^2, \quad (7)$$

where $\tilde{I}_i(\mathbf{p})$ denotes the measured X-ray intensity on detector i . Each region (or part) is assigned one trainable parameter μ_k , representing its LAC. The background region (air)

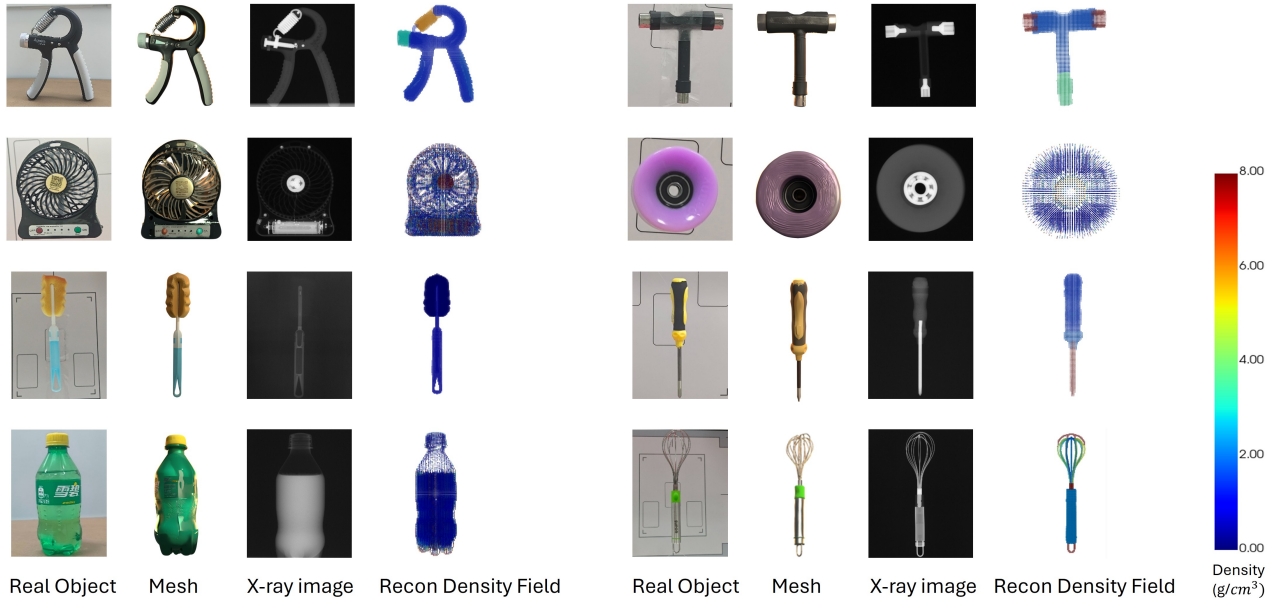


Figure 5. **Gallery of XDen-1K.** Our XDen-1K dataset contains RGB images, scanned biplanar X-ray images, and approximately reconstructed density fields.

is fixed as μ_{air} . Using a differentiable forward-projection operator, the gradients $\partial I_i(\mathbf{p})/\partial \mu_k$ are computed automatically and the parameters μ are optimized via Adam until convergence.

This formulation transforms the original high-dimensional inverse problem of estimating a dense field $\mu(\mathbf{x})$ into a low-dimensional optimization over a compact parameter set μ . The part-segmented mask serves as a powerful geometric prior that constrains the solution space, effectively regularizing the reconstruction and enabling tractable and physically consistent 3D recovery from only two biplanar X-ray projections.

3.5. Evaluation of Reconstruction Fidelity

To assess the fidelity of our coarse density estimation algorithm used to construct the dataset, we collected additional CT scans as reference data for quantitative analysis. However, metal artifacts in CT images can substantially distort the reconstructed attenuation values, leading to unreliable reference measurements. Therefore, we divide the subjects into two categories: (1) those with no metal artifacts or only minor artifacts (including mirror, glue stick, potted plant, etc.), and (2) those with severe metal artifacts (including pliers, utility knives, mobile phones, etc.). For each subject, we extract the segmented anatomical region from the CT scan and compute its voxel-wise density. These CT-derived values are then compared against the predicted density obtained from our optimized algorithm. We report the **mean absolute percentage error (MAPE)** as the evaluation metric, as summarized in Table 2.

Table 2. Voxel-wise MAPE of density field between our method and CT across all objects.

Category / Mean	Object	MAPE
Non-metal (Mean: 0.4795)	Mirror	0.3779
	Bulb	1.6813
	Plant	0.4491
	Glue	0.4673
	Pen	0.2591
	Bottle	0.3472
	Toothbrush	0.2244
	Milk	0.0294
Metal (Mean: 0.7741)	Phone	0.6895
	Pump	3.0104
	Pliers	0.3302
	Wrench	0.4300
	Awl	0.4665
	Swiss Knife	0.1482
	Glasses	0.3436

Results in the non-metallic region demonstrate that our proposed biplanar approximation algorithm can effectively reconstruct the 3D density field. Furthermore, in data with larger metallic components, although metal artifacts cause some deviation in values, the trend of our reconstructed density field is consistent with that in CT. Compared to CT reconstruction methods, this significantly reduces cost and time while obtaining a relatively reliable density field.

4. Applications and Experiments on XDen-1K

Building on XDen-1K, we introduce two downstream tasks: **X-ray conditioned volumetric segmentation** and **center-of-mass-aware robot manipulation**. We argue that X-ray

imaging is a key modality for spatial perception, providing rich depth cues and material priors. When combined with volumetric density fields, XDen-1K enables physically grounded reasoning about objects and supports a broad range of downstream applications.

4.1. X-ray conditioned volumetric segmentation

Building on the strong priors in material and internal structure provided by X-ray images, we take it as the conditioning modality and extend the part-aware feature learning of PartField [31] to the volumetric domain. Conditioned on biplanar X-ray images, **X-Field** is trained on a synthetic dataset to predict a dense volumetric field, which is then clustered into part-level segments. Evaluated on both synthetic and real data, X-Field consistently outperforms the original PartField.

4.1.1. Synthetic data pipeline

We construct a synthetic dataset of 7.6K objects for training. It is built on PartNeXt [42], a hierarchical 3D part dataset, where we develop an SDF-based method to separate the surface and interior regions of each part and use a Vision–Language Model (VLM) to assign a material label to every part. For each material, we record its density and attenuation coefficient and map the material labels to these physical properties. Following the Lambert–Beer law in Eq. 2, we then render corresponding X-ray images for every object in a simulated environment.

4.1.2. Material-based volumetric segmentation

PartField takes an input point cloud P , extracts features with PVCNN, and maps them onto a triplane representation. A transformer decoder predicts triplane features L_{tri} , which are then projected back to all points.

On top of this backbone, X-ray conditioning is introduced as follows. The biplanar X-ray images I_X are encoded into features L_X . Because X-ray appearance is highly scale-dependent, the physical scale λ is also provided, and FiLM is applied to normalize L_X into a unified latent space. The resulting X-ray features L_X are injected into the triplane features L_{tri} via cross-attention:

$$\tilde{L}_{\text{tri}} = \text{CrossAttention}(L_{\text{tri}}, \text{Encoder}(I_X)). \quad (8)$$

The objective is to predict the density at each location in the voxel grid. To this end, query points P_{query} are randomly sampled in the volume, and a density MLP head regresses their densities D_P . Supervision is provided by an ℓ_2 loss between the predicted densities and the ground-truth densities from the synthetic volumetric fields.

Biplanar X-ray input naturally leads to missing-view artifacts. To alleviate this, an additional X-ray image is decoded from the features associated with the third plane, and

Method	Synthetic Data IoU \uparrow	Real Data IoU \uparrow
PartField	53.185	38.410
X-Field (Ours)	72.645	49.251

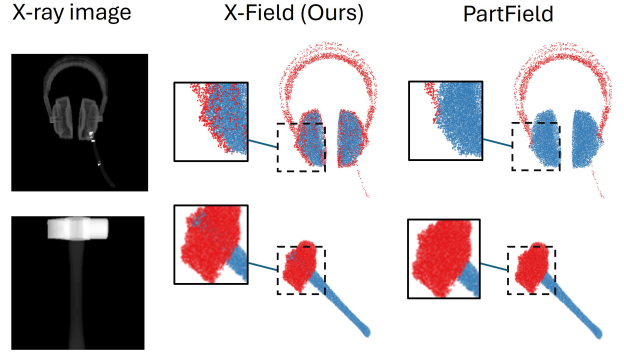


Figure 6. Comparison of IoU and qualitative segmentation results on synthetic and real data for PartField and X-Field.

an MSE loss with respect to the corresponding ground-truth X-ray image is imposed. This auxiliary reconstruction task regularizes 3D feature learning and encourages more complete volumetric reasoning.

Finally, k -means clustering is applied to the predicted densities of the query points, partitioning the volume into regions whose points share similar density values and yielding a material-aware volumetric segmentation.

4.1.3. Evaluation on X-ray conditioned segmentation

The volumetric segmentation performance of the original PartField and the proposed X-Field is evaluated on both synthetic and real data. As shown in Fig. 6, conditioning on biplanar X-ray images leads to higher IoU scores and better volumetric segmentations.

4.2. Robot Manipulation

The perception of an object’s center of mass is fundamental for achieving physically stable and dynamically consistent manipulation. Beyond geometric reasoning, understanding the relationship between the center of mass, external forces, and contact points allows a robot to anticipate rotation, slippage, and tipping during interaction.

To study how the center of mass influences manipulation outcomes, we conduct three representative experiments on a Franka Emika Panda robotic arm equipped with a parallel gripper.

Pick. In the hammer grasping task (Fig. 7, top), the robot attempts to lift the object from different grasp points. When the grasp point lies close to the center of mass, the gravitational moment is small, and the hammer can be lifted sta-

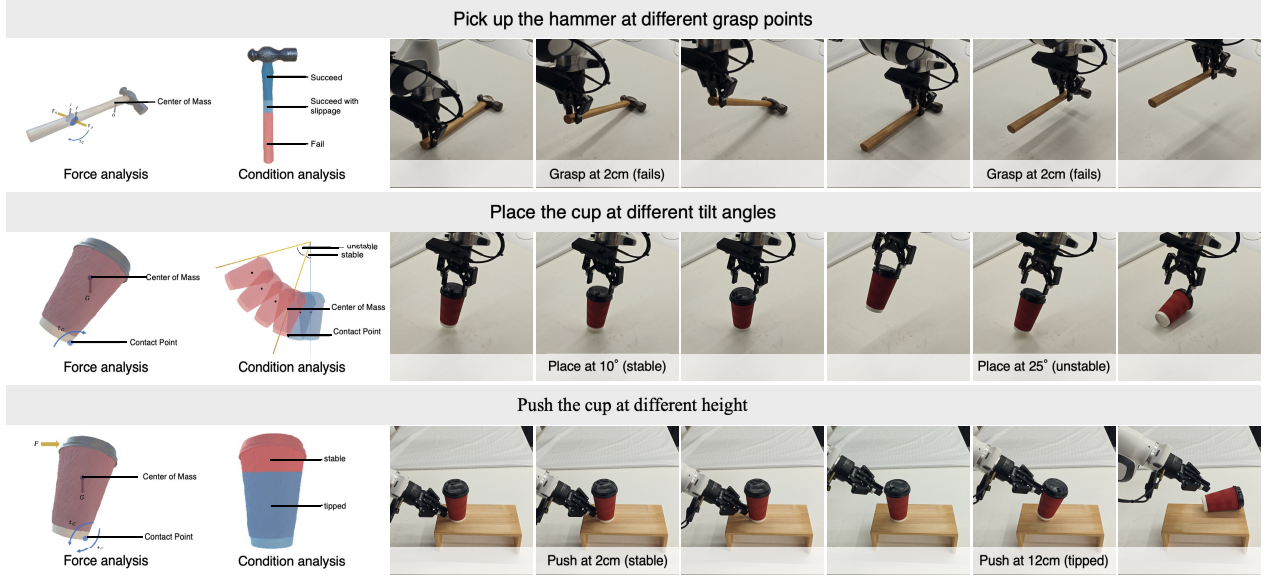


Figure 7. Effect of the object’s center of mass on manipulation stability. Left: force and stability analysis. Right: real-robot executions. **Top:** hammer grasping; grasping near the center of mass is stable, while grasping near the tip fails due to a larger gravitational moment. **Middle:** cup placement; a small tilt (10°) is stable, whereas a larger tilt (25°) shifts the center-of-mass projection outside the support region and causes tipping. **Bottom:** cup pushing; pushing below the center of mass (2 cm) is stable, while pushing above it (12 cm) generates an overturning moment and tips the cup.

bly. As the grasp point moves farther away, the lever arm between the grasp point and the center of mass increases. This produces a larger torque that exceeds the frictional support at the contacts, causing the hammer to rotate around the grasp axis and resulting in grasp failure. The conceptual model in Fig. 7 illustrates how removing external stabilization leads the hammer to rotate immediately due to this torque imbalance.

Place. In the tilted placement task (Fig. 7, middle), the robot places a cup on the table with different initial tilt angles. The object’s behavior depends on whether the projection of the center of mass lies within the support region. A small tilt keeps the projection inside the support polygon, generating a restoring moment that brings the cup upright. At larger tilt angles, the projection shifts outside the support area, and the resulting overturning moment causes the cup to fall. The simplified force diagram in Fig. 7 visualizes how the relative position between the center of mass and the contact point determines stability.

Push. When pushing a cup horizontally at different heights (Fig. 7, bottom), the applied force creates a moment around the object’s center of mass. Pushing below the center of mass induces a small moment, so the cup primarily translates without rotating. Pushing above the center of mass produces a much larger overturning moment that tips the cup. Once the cup begins to rotate, gravity again influences the outcome: the object may return to an upright position or continue tipping depending on the new alignment between the center of mass and the contact point. The dia-

grams in Fig. 7 show how force direction, pushing height, and the center of mass jointly affect the tipping behavior.

These experiments indicate that reasoning about the object’s center of mass plays an important role in improving grasping, placement, and pushing performance. Leveraging this physical understanding can contribute to more stable behaviors and more reliable interaction with diverse objects in real-world settings.

5. Conclusion

We presented **XDden-1K**, a large-scale real-world dataset that provides paired biplanar X-rays and dense 3D density fields. We proposed an X-ray optimization framework that leverages shape and segmentation priors to recover piecewise-constant densities from only two projections, transforming an otherwise ill-posed problem into a tractable estimation task. Although perfect pixel-level alignment with the real X-ray pose is unattainable during optimization, comparisons with CT show that the recovered density fields are sufficiently accurate for downstream applications. We further introduced two benchmark tasks: an X-ray conditioned volumetric segmentation network, and a center-of-mass-aware robot manipulation task. Experimental results demonstrate the broad potential of XDden-1K for advancing perception and robotics. We argue that density fields and X-ray maps represent a promising new class of physically grounded visual representations, opening new directions for X-ray-based understanding, reconstruction, and interaction.

References

- [1] Mahmoud Ahmed, Xiang Li, Arpit Prajapati, and Mohamed Elhoseiny. 3dcompat200: Language-grounded compositional understanding of parts and materials of 3d shapes, 2025. [2](#), [3](#)
- [2] Veronica E Arriola-Rios, Puren Guler, Fanny Ficuciello, Danica Kragic, Bruno Siciliano, and Jeremy L Wyatt. Modeling of deformable objects for robotic manipulation: A tutorial and review. *Frontiers in Robotics and AI*, 7:82, 2020. [2](#)
- [3] Anton Bakhtin, Laurens van der Maaten, Justin Johnson, Laura Gustafson, and Ross Girshick. Phyre: A new benchmark for physical reasoning. *arXiv:1908.05656*, 2019. [2](#)
- [4] Britt-Isabelle Berg, Aurélien Laville, Delphine S Courvoisier, Philippe Rouch, and Thomas Schouman. Experiences with a new biplanar low-dose x-ray device for imaging the facial skeleton: A feasibility study. *PloS one*, 15(7): e0235032, 2020. [3](#)
- [5] Martin J Berger and John Howard Hubbell. Xcom: Photon cross sections on a personal computer. Technical report, National Bureau of Standards, Washington, DC (USA). Center for Radiation ..., 1987. [5](#)
- [6] Yuanhao Cai, Jiahao Wang, Alan Yuille, Zongwei Zhou, and Angtian Wang. Structure-aware sparse-view x-ray 3d reconstruction. In *Proceedings of the IEEE/CVF conference on computer vision and pattern recognition*, pages 11174–11183, 2024. [3](#)
- [7] Ziang Cao, Zhaoxi Chen, Liang Pan, and Ziwei Liu. Physx-3d: Physical-grounded 3d asset generation. *ArXiv*, abs/2507.12465, 2025. [2](#)
- [8] Ziang Cao, Fangzhou Hong, Zhaoxi Chen, Liang Pan, and Ziwei Liu. Physx-anything: Simulation-ready physical 3d assets from single image, 2025. [2](#)
- [9] Yue Chang, Mengfei Liu, Zhecheng Wang, Peter Yichen Chen, and Eitan Grinspun. Lifting the winding number: Precise discontinuities in neural fields for physics simulation. In *ACM SIGGRAPH 2025 Conference Papers*, 2025. [2](#)
- [10] Yuepeng Chen, Yue Gao, Xiangling Fu, Yingyin Chen, Ji Wu, Chenyi Guo, and Xiaodong Li. Automatic 3d reconstruction of vertebrae from orthogonal bi-planar radiographs. *Scientific Reports*, 14(1):16165, 2024. [3](#)
- [11] Christopher Choy, JunYoung Gwak, and Silvio Savarese. 4d spatio-temporal convnets: Minkowski convolutional neural networks. In *Proceedings of the IEEE/CVF conference on computer vision and pattern recognition*, pages 3075–3084, 2019. [3](#)
- [12] Angela Dai, Angel X Chang, Manolis Savva, Maciej Halber, Thomas Funkhouser, and Matthias Nießner. Scannet: Richly-annotated 3d reconstructions of indoor scenes. In *Proceedings of the IEEE conference on computer vision and pattern recognition*, pages 5828–5839, 2017. [3](#)
- [13] Zheng Dang, Jialu Huang, Fei Wang, and Mathieu Salzmann. Openmaterial: A large-scale dataset of complex materials for 3d reconstruction, 2025. [2](#)
- [14] Boyang Deng, Kyle Genova, Soroosh Yazdani, Sofien Bouaziz, Geoffrey Hinton, and Andrea Tagliasacchi. Cvxnet: Learnable convex decomposition. In *Proceedings of the IEEE/CVF conference on computer vision and pattern recognition*, pages 31–44, 2020. [3](#)
- [15] Lee A Feldkamp, Lloyd C Davis, and James W Kress. Practical cone-beam algorithm. *Journal of the Optical Society of America A*, 1(6):612–619, 1984. [3](#)
- [16] Daniel Thomas Ginat and Rajiv Gupta. Advances in computed tomography imaging technology. *Annual review of biomedical engineering*, 16(1):431–453, 2014. [3](#)
- [17] Jack L Glover and Lawrence T Hudson. An objectively-analyzed method for measuring the useful penetration of x-ray imaging systems. *Measurement Science and Technology*, 27(6):065402, 2016. [3](#)
- [18] Benjamin Graham, Martin Engelcke, and Laurens Van Der Maaten. 3d semantic segmentation with submanifold sparse convolutional networks. In *Proceedings of the IEEE conference on computer vision and pattern recognition*, pages 9224–9232, 2018. [3](#)
- [19] Minghao Guo, Bohan Wang, Pingchuan Ma, Tianyuan Zhang, Crystal Elaine Owens, Chuang Gan, Joshua B. Tenenbaum, Kaiming He, and Wojciech Matusik. Physically compatible 3d object modeling from a single image. In *Advances in Neural Information Processing Systems*, pages 119260–119282. Curran Associates, Inc., 2024. [2](#)
- [20] Bei Huang and Yuru Pei. Generalizable structure-aware inf: Biplanar-view ct reconstruction via disentangled implicit neural field. In *Proceedings of the Asian Conference on Computer Vision*, pages 699–715, 2024. [3](#)
- [21] Tianyu Huang, Yihan Zeng, Hui Li, Wangmeng Zuo, and Rynson WH Lau. Dreamphysics: Learning physical properties of dynamic 3d gaussians with video diffusion priors. *arXiv preprint arXiv:2406.01476*, 2024. [2](#)
- [22] Xin Huang, Tengfei Wang, Ziwei Liu, and Qing Wang. Material anything: Generating materials for any 3d object via diffusion, 2024. [2](#)
- [23] Yun Su Jeong, Hye Bin Yoo, and Il Yong Chun. Dx2ct: Diffusion model for 3d ct reconstruction from bi or monoplanar 2d x-ray (s). In *ICASSP 2025-2025 IEEE International Conference on Acoustics, Speech and Signal Processing (ICASSP)*, pages 1–5. IEEE, 2025. [3](#)
- [24] Hanxiao Jiang, Hao-Yu Hsu, Kaifeng Zhang, Hsin-Ni Yu, Shenlong Wang, and Yunzhu Li. Phystwin: Physics-informed reconstruction and simulation of deformable objects from videos, 2025. [2](#)
- [25] Krishna Kumar, Jeffrey Salmond, Shyamini Kularathna, Christopher Wilkes, Ezra Tjung, Giovanna Biscontin, and Kenichi Soga. Scalable and modular material point method for large-scale simulations, 2019. [2](#)
- [26] Daeun Kyung, Kyungmin Jo, Jaegul Choo, Joonseok Lee, and Edward Choi. Perspective projection-based 3d ct reconstruction from biplanar x-rays. In *ICASSP 2023-2023 IEEE International Conference on Acoustics, Speech and Signal Processing (ICASSP)*, pages 1–5. IEEE, 2023. [3](#)
- [27] Long Le, Ryan Lucas, Chen Wang, Chuhao Chen, Dinesh Jayaraman, Eric Eaton, and Lingjie Liu. Pixie: Fast and generalizable supervised learning of 3d physics from pixels. *ArXiv*, abs/2508.17437, 2025. [2](#)

- [28] Shiqian Li, Kewen Wu, Chi Zhang, and Yixin Zhu. I-phyre: Interactive physical reasoning. In *Proceedings of the International Conference on Learning Representations (ICLR)*. OpenReview.net, 2024. 2
- [29] Xuan Li, Yi-Ling Qiao, Peter Yichen Chen, Krishna Murthy Jatavallabhula, Ming Lin, Chenfanfu Jiang, and Chuang Gan. Pac-nerf: Physics augmented continuum neural radiance fields for geometry-agnostic system identification. *ArXiv*, abs/2303.05512, 2023. 2
- [30] Yuan Lin and Ehsan Samei. An efficient polyenergetic sart (psart) reconstruction algorithm for quantitative myocardial ct perfusion. *Medical physics*, 41(2):021911, 2014. 3
- [31] Minghua Liu, Mikaela Angelina Uy, Donglai Xiang, Hao Su, Sanja Fidler, Nicholas Sharp, and Jun Gao. Partfield: Learning 3d feature fields for part segmentation and beyond. *ArXiv*, abs/2504.11451, 2025. 3, 7
- [32] Xiaohe Ma, Xianmin Xu, Leyao Zhang, Kun Zhou, and Hongzhi Wu. Opensvbrdf: A database of measured spatially-varying reflectance. 42(6), 2023. 2
- [33] Elias Melhem, Ayman Assi, Rami El Rachkidi, and Ismat Ghanem. Eos® biplanar x-ray imaging: concept, developments, benefits, and limitations. *Journal of children's orthopaedics*, 10(1):1–14, 2016. 3
- [34] Ben Mildenhall, Pratul P. Srinivasan, Matthew Tancik, Jonathan T. Barron, Ravi Ramamoorthi, and Ren Ng. Nerf: Representing scenes as neural radiance fields for view synthesis, 2020. 3
- [35] Johan Nuyts, Bruno De Man, Jeffrey A Fessler, Wojciech Zbijewski, and Freek J Beekman. Modelling the physics in the iterative reconstruction for transmission computed tomography. *Physics in Medicine & Biology*, 58(12):R63, 2013. 3
- [36] Thomas Rodet, Frédéric Noo, and Michel Defrise. The cone-beam algorithm of feldkamp, davis, and kress preserves oblique line integrals. *Medical physics*, 31(7):1972–1975, 2004. 3
- [37] Gregory P Slota, Moon Suk Suh, Mark L Latash, and Vladimir M Zatsiorsky. Stability control of grasping objects with different locations of center of mass and rotational inertia. *Journal of motor behavior*, 44(3):169–178, 2012. 2
- [38] Wenjuan Sun, Daniel R Symes, Ceri M Brenner, Michael Böhnelt, Stephen Brown, Mark N Mavrogordato, Ian Sinclair, and Michael Salamon. Review of high energy x-ray computed tomography for non-destructive dimensional metrology of large metallic advanced manufactured components. *Reports on Progress in Physics*, 85(1):016102, 2022. 3
- [39] George Tang, William Zhao, Logan Ford, David Benhaim, and Paul Zhang. Segment any mesh: Zero-shot mesh part segmentation via lifting segment anything 2 to 3d. *ArXiv*, abs/2408.13679, 2024. 3
- [40] Hsiao-Yu Tung, Mingyu Ding, Zhenfang Chen, Daniel Bear, Chuang Gan, Joshua B. Tenenbaum, Daniel LK Yamins, Judith E Fan, and Kevin A. Smith. Physion++: Evaluating physical scene understanding that requires online inference of different physical properties, 2023. 2
- [41] Jianyuan Wang, Minghao Chen, Nikita Karaev, Andrea Vedaldi, Christian Rupprecht, and David Novotny. Vggt: Visual geometry grounded transformer, 2025. 2
- [42] Penghao Wang, Yiyang He, Xin Lv, Yukai Zhou, Lan Xu, Jingyi Yu, and Jiayuan Gu. Partnext: A next-generation dataset for fine-grained and hierarchical 3d part understanding. 2025. 7
- [43] Qing Wu, Ruimin Feng, Hongjiang Wei, Jingyi Yu, and Yuyao Zhang. Self-supervised coordinate projection network for sparse-view computed tomography. *IEEE Transactions on Computational Imaging*, 9:517–529, 2023. 3
- [44] Jianfeng Xiang, Zelong Lv, Sicheng Xu, Yu Deng, Ruicheng Wang, Bowen Zhang, Dong Chen, Xin Tong, and Jiaolong Yang. Structured 3d latents for scalable and versatile 3d generation. *arXiv preprint arXiv:2412.01506*, 2024. 2
- [45] Ziyang Xie, Zhizheng Liu, Zhenghao Peng, Wayne Wu, and Bolei Zhou. Vid2sim: Realistic and interactive simulation from video for urban navigation. *2025 IEEE/CVF Conference on Computer Vision and Pattern Recognition (CVPR)*, pages 1581–1591, 2025. 2
- [46] Xinli Xu, Wenhong Ge, Dicong Qiu, Zhifei Chen, Dongyu Yan, Zhuoyun Liu, Haoyu Zhao, Hanfeng Zhao, Shunsi Zhang, Junwei Liang, and Ying-Cong Chen. Gaussianproperty: Integrating physical properties to 3d gaussians with Imms. *ArXiv*, abs/2412.11258, 2024. 2
- [47] Zhenjia Xu, Jiajun Wu, Andy Zeng, Joshua B. Tenenbaum, and Shuran Song. Densephysnet: Learning dense physical object representations via multi-step dynamic interactions, 2019. 2
- [48] Kaixin Yao, Longwen Zhang, Xinhao Yan, Yan Zeng, Qixuan Zhang, Lan Xu, Wei Yang, Jiayuan Gu, and Jingyi Yu. Cast: Component-aligned 3d scene reconstruction from an rgb image, 2025. 2
- [49] Kexin Yi, Chuang Gan, Yunzhu Li, Pushmeet Kohli, Jiajun Wu, Antonio Torralba, and Joshua B. Tenenbaum. CLEVRER: collision events for video representation and reasoning. In *ICLR*, 2020. 2
- [50] Xingde Ying, Heng Guo, Kai Ma, Jian Wu, Zhengxin Weng, and Yefeng Zheng. X2ct-gan: reconstructing ct from biplanar x-rays with generative adversarial networks. In *Proceedings of the IEEE/CVF conference on computer vision and pattern recognition*, pages 10619–10628, 2019. 3
- [51] Albert J. Zhai, Yuan Shen, Emily Y. Chen, Gloria X. Wang, Xinlei Wang, Sheng Wang, Kaiyu Guan, and Shenlong Wang. Physical property understanding from language-embedded feature fields. *2024 IEEE/CVF Conference on Computer Vision and Pattern Recognition (CVPR)*, pages 28296–28305, 2024. 2
- [52] Guanqi Zhan, Xianzheng Ma, Weidi Xie, and Andrew Zisserman. Inferring dynamic physical properties from video foundation models, 2025. 2
- [53] Longwen Zhang, Qixuan Zhang, Haoran Jiang, Yinyao Bai, Wei Yang, Lan Xu, and Jingyi Yu. Bang: Dividing 3d assets via generative exploded dynamics. *ACM Transactions on Graphics (TOG)*, 44:1–21, 2025. 3
- [54] Yuchen Zhou, Jiayuan Gu, Tung Yen Chiang, Fanbo Xiang, and Hao Su. Point-sam: Promptable 3d segmentation model for point clouds. *ArXiv*, abs/2406.17741, 2024. 3